Title

Understanding the Oxygen Evolution Reaction Mechanism on CoO x using Operando Ambient-Pressure X-ray Photoelectron Spectroscopy

Journal

Journal of the American Chemical Society, 139(26)

ISSN

0002-7863

Authors

Favaro, Marco

Yang, Jinhui

Nappini, Silvia

et al.

Publication Date

2017-07-05

DOI

10.1021/jacs.7b03211

Peer reviewed

Understanding the oxygen evolution reaction mechanism on CoO_x using *operando* ambient pressure X-ray photoelectron spectroscopy

Marco Favaro*[1,2,3‡], Jinhui Yang[2,3], Silvia Nappini[4], Elena Magnano[4], Francesca M. Toma[2,3], Ethan J. Crumlin[1], Junko Yano*[2,3,5], and Ian D. Sharp*[2,3]

[1]Advanced Light Source, Lawrence Berkeley National Laboratory, One Cyclotron Rd., Berkeley, CA 94720, USA, [2]Joint Center for Artificial Photosynthesis, Lawrence Berkeley National Laboratory, One Cyclotron Rd., Berkeley, CA 94720, USA, [3]Chemical Sciences Division, Lawrence Berkeley National Laboratory, One Cyclotron Rd., Berkeley, CA 94720, USA, [4]IOM-CNR, Laboratorio TASC, Area Science Park Basovizza, s.s. 14 km 163, 5 Basovizza, 34149 Trieste, Italy, [5]Molecular Biophysics and Integrated Bioimaging Division, Lawrence Berkeley National Laboratory, One Cyclotron Rd., Berkeley, CA 94720.

KEYWORDS: Water splitting, cobalt oxide photoelectrocatalysts, operando spectroscopy, ambient pressure XPS, oxygen evolution reaction mechanism

ABSTRACT: Photoelectrochemical water splitting is a promising approach for renewable production of hydrogen from solar energy and requires interfacing advanced water splitting catalysts with semiconductors. Understanding the mechanism of function of such electrocatalysts at the atomic scale and under realistic working conditions is a challenging, yet important, task for advancing efficient and stable function. This is particularly true for the case of oxygen evolution catalysts and, here, we study a highly active $Co_3O_4/Co(OH)_2$ biphasic electrocatalyst on Si by means of *operando* ambient pressure X-ray photoelectron spectroscopy performed at the solid/liquid electrified interface. Spectral simulation and multiplet fitting reveal that the catalyst undergoes chemical-structural transformations as a function of the applied anodic potential, with complete conversion of the $Co(OH)_2$ and partial conversion of the spinel Co_3O_4 phases to CoO(OH) under pre-catalytic electrochemical conditions. Furthermore, we observe new spectral features in both Co 2*p* and O 1*s* core level regions to emerge under oxygen evolution reaction conditions on CoO(OH). The *operando* photoelectron spectra support assignment of these newly observed features to highly active Co^{4+} centers under catalytic conditions. Comparison of these results to those from a pure phase spinel Co_3O_4 catalyst supports this interpretation and reveals that the presence of $Co(OH)_2$ enhances catalytic activity by promoting transformations to CoO(OH). The direct investigation of electrified interfaces presented in this work can be extended to different materials under realistic catalytic conditions, thereby providing a powerful tool for mechanism discovery and an enabling capability for catalyst design.

Introduction

Sustainable solutions are required to mitigate the impact of increasing world energy demand on the environment and avoid depletion of natural energy sources (1). While transduction of solar energy to electricity has already made a significant impact on the renewable energy sector, the intermittent nature of sunlight imposes critical storage challenges (2, 3, 4, 5, 6). Furthermore, addressing broader energy needs, particularly in transportation, requires new technologies for the next generation of renewable fuels. Within this context, (photo)electrochemical conversion of sunlight to hydrogen – or other chemical fuels – represents an appealing approach to both solar energy conversion and high energy density storage. An essential step in such artificial photosystems is the oxygen evolution reaction (OER), in which the protons and electrons required for the fuel formation reaction are harnessed from water (2-7, 8, 9). However, OER pathways can be complex and impose significant kinetic bottlenecks. To address this challenge, increasing efforts have been devoted to developing OER catalysts possessing high activity, long-term durability, and low cost, a combination of attributes that is most commonly obtained with first row transition metal oxides (10, 11, 12, 13, 14, 15, 16, 17).

Among OER catalysts, Co oxides (CoO_x) have been shown to possess desirable activity over a broad range of pH values (12, 16, 18), from near-neutral to alkaline conditions. Substantial work has been aimed at understanding relationships between structure, mechanism, and activity (19, 20, 21, 22, 23, 24, 25, 26). This has led to novel insights into the nature of catalytically active sites at the atomic scale (19, 25, 27, 28), as well as the role of structural transformations from the resting to the catalytic state (29, 30, 31, 32). Recently, observations that highly disordered or amorphous materials can exhibit enhanced catalytic activity relative to their crystalline counterparts (28, 32, 33, 34, 35, 36) has ignited significant interest in developing and characterizing such systems. For example, several recent studies used electrochemical methods to show that the bulk region of CoO_x-based catalysts can be active for OER owing to the formation of a highly accessible CoO(OH) layered structure, in which water and electrolyte can efficiently intercalate (12, 19, 25, 31, 36, 37). In addition, we

recently demonstrated that biphasic $Co(OH)_2/Co_3O_4$ films formed via plasma-enhanced atomic layer deposition (PE-ALD) can be specifically engineered for integration with semiconductor light absorbers to promote efficient and stable light-driven oxygen evolution (37).

Up to now, such systems have been mostly probed using *ex situ* spectroscopic methods, many of which remove or are not sensitive to the liquid phase and do not support applied potentials. As these conditions are far from operational electrochemical environments, only limited information about the active solid/liquid interface can be inferred. To advance our ability to tailor novel materials for use in functional devices, it is necessary to achieve a mechanistic understanding of how the chemical and electronic structure of the catalyst, the electrochemical environment, and reaction intermediates/products depend upon one another. To gain this knowledge, novel experimental techniques and innovative strategies have been developed, with the aim of unravelling the (electro)chemistry at solid/liquid electrified interfaces in realistic liquid environments and under applied potentials.

For the case of CoO_x, it has been shown that ordered systems can undergo phase transitions to disordered states under catalytic operation. Bergmann and co-workers recently investigated spinel Co_3O_4 using *in situ* X-ray absorption spectroscopy (XAS) and X-ray diffraction (XRD), demonstrating that transformation to the active (catalytic) phase is accompanied by reversible amorphization of a sub-nm thick near-surface region of Co_3O_4 to $CoO_x(OH)_y$ (28, 31). The proposed mechanism presents an interesting view of (electro)catalysis using dynamic systems, such as late transition metal oxides, whereby increasing concentrations of catalytically active sites within the bulk can contribute to higher overall activity per geometric area. Additional evidence for these processes was provided by *in situ* XAS to monitor the chemical evolution of the Co centers, as well as their local structure, during the OER (27, 32), showing that the active phase derives from the oxidative conversion of CoO_x to CoO(OH).

Despite recent advances, nearly all *in situ* studies of energy-related materials have been performed using bulk sensitive spectroscopies, such as hard X-ray XAS and XRD. The recent coupling of operational systems with surface sensitive techniques, such as X-ray photoelectron spectroscopy (XPS), provides significant opportunity for shedding new light on phenomena occurring at the solid/liquid electrified interface (38, 39, 40, 41, 42, 43, 44, 45, 46, 47, 48). In this work, we study, under *operando* conditions, the chemical and structural evolution of different conformal CoO_x catalyst layers formed by plasma-enhanced atomic layer deposition (PE-ALD) on p^+-Si substrates (37) as a function of the applied electrochemical potential. In a previous work, we have demonstrated that the biphasic $Co(OH)_2/Co_3O_4$-Si system yields best reported performance characteristics for crystalline Si-based photoanodes (37). Therefore, the chemical and electronic property characterization of the catalyst outer layer under operating conditions provided in the present work allows for identification of active catalytic surface species and a path to a complete experimental description of the OER mechanism on Co-based oxides. To perform a detailed surface and near-surface spectroscopic investigation, we have used ambient pressure X-ray photoelectron spectroscopy (APXPS) coupled with intermediate energy, or "tender", X-rays ($h\nu$ = 4.0 keV). Taking advantage of the high photoelectron kinetic energy (49, 50) it is possible to probe 10 - 30 nm of a liquid phase and 2 - 10 nm of a solid phase, while simultaneously undergoing electrochemical reactions (39, 42-44, 46, 48).

Previously, we observed a significant improvement of OER electrocatalytic activity in a biphasic CoO_x system, in which a disordered outer-surface layer of $Co(OH)_2$ is introduced atop a nanocrystalline spinel Co_3O_4 phase via PE-ALD, relative to pure phase spinel Co_3O_4 (37). However, the electrochemical and *ex situ* spectroscopic measurements utilized in that study were incapable of characterizing the extent of conversion from $Co(OH)_2$ to CoO(OH), the degree to which spinel Co_3O_4 may undergo parallel chemical transformations, the composition of the film under real operational conditions, or the validity of the current mechanistic models for OER on CoO_x formed via PE-ALD. Here, we confirm that the $Co(OH)_2$ surface layer promotes chemical and structural transformation, including complete oxidative conversion to CoO(OH), a phase that can support high concentrations of catalytically active sites distributed throughout its entire thickness. Furthermore, while we observe partial conversion of the underlying spinel Co_3O_4 to CoO(OH), the layer is sufficiently thick to provide a stable interface to the underlying semiconductor substrate, which is a key requirement for solar-driven systems in which conformal catalyst layers are also used for corrosion protection. Under oxygen evolution conditions, we observe the development of a new spectral component in the Co 2*p* and O 1*s* photoelectron peaks, which we assigned to the presence of Co^{4+} centers.

Finally, to prove the crucial role played by the initial presence of the $Co(OH)_2$ disordered layer, we have investigated a second catalytic system composed of a single phase layer of spinel Co_3O_4, also prepared by PE-ALD and previously found to have significantly lower catalytic activity than the biphasic system (37). Our findings show that the chemical resilience of this structure greatly inhibits the oxidative conversion to the highly active oxy-hydroxide phase, resulting in a low OER activity compared to the biphasic system (37). These results indicate that extremely thin biphasic catalyst films, with thicknesses on the single digit nanometer scale, can be tailored to provide high activity, while also providing a stable interface to underlying substrates, thus making them suitable for protection of semiconductor light absorbers against chemical attack.

Results

Operando spectroscopic investigation of the biphasic CoO_x system

Investigation of atomic layer deposited (ALD) biphasic CoO_x catalyst were performed under oxygen evolution reaction (OER) conditions using the experimental set up shown schematically in **Figure 1a**. The electrochemical cell was based on a three electrode configuration in which the investigated sample was used as the working electrode (WE), a polycrystalline Pt foil was used as the counter electrode, and a $Ag/AgCl/Cl^-_{(sat.)}$ electrode was used as the reference. The *operando* measurements were performed in 1.0 M KOH aqueous solution in a reduced pressure H_2O-saturated environment (~18 Torr) at room temperature (~298 K). For a better comparison with the literature, the measured potential is also reported vs. the reversible hydrogen electrode (RHE). Unless otherwise stated, all the potentials reported in this work are referred to this reference in the 1 M KOH aqueous solution (pH 13.8). The obtained cyclic voltammogram (CV), measured in the APXPS setup at a scan rate of 20 mV s^{-1}, is reported in **Figure 1b** and a schematic illustration of the investigated biphasic CoO_x catalyst is shown in **Figure 1c**. After the "dip and pull" procedure described in the methods

section (39, 42-46, 48), a 19.4 ± 0.7 nm nanometer thick electrolyte layer, as determined using the inverse Beer-Lambert relation (39, 42-44, 46, 48), was obtained on the WE surface and provided a continuous conduction path to the bulk electrolyte. This configuration enabled study of the solid/liquid interface as a function of the applied electrochemical potential (39, 42-44, 46, 48).

To accurately trace the evolution of the surface chemistry, the O 1*s*, Co 2*p*, and valence band (VB) spectral features were acquired by following a systematic measurement sequence. After mounting the three electrodes, the analysis chamber was evacuated to approximately 10^{-5} Torr. Then, high purity N_2 was leaked into the chamber until the pressure reached 10 Torr and APXPS was performed under dry conditions, hereafter referred to as "pristine conditions". Next, the chamber was vented, a beaker containing the electrolyte was inserted into the analysis chamber, and the system was slowly pumped until the electrolyte vapor pressure (~18 Torr) at room temperature (~298 K) was reached. APXPS was then measured in this H_2O-saturated environment, hereafter referred to as "hydrated conditions". The sample was then immersed into the 1.0 M KOH and partially retracted from the solution. Once a stable electrolyte layer was formed at the analysis spot, APXPS was performed at the open circuit potential (U_{OCP}) and then as a function of the applied electrochemical potential. These measurements, collected after the dip and pull procedure, are hereafter referred to as "electrochemical conditions".

By measuring core level binding energy (BE) shifts of elements present in the liquid layer, it is possible to experimentally determine the local potential at the analysis position as a function of the applied potential (42-44, 46, 48). As shown in **Figure 2a**, the O 1*s* core level region is characterized by multiple spectral features, with contributions from both the multilayer water structure and the CoO_x film. The two highest binding energy components, at approximately 536 and 534 eV, can be assigned to oxygen in gas phase water (GPW) and liquid phase water (LPW), respectively (39, 42-44, 46, 48). Under an applied electrochemical potential, *U*, the binding energy of the bulk electrolyte, $BE_{electrolyte}$, shifts with respect to the Femi level of the sample, which is grounded to the analyzer, as schematically depicted in **Figure 1a**. In the absence of series resistance effects, this shift is expected to obey the relation: $BE_{electrolyte} = BE_0 - eU$, where BE_0 is defined as the BE of the LPW component at U_{OCP}. As shown in **Figure 2b**, the bias-induced BE shift exhibits the ideal unity-slope linear relationship with electrochemical potential, indicating that polarization losses due to series resistance are minimal for current densities generated in the measured potential range.

Information regarding the chemical and electronic states of the catalytic CoO_x films, as well as their changes under different conditions, is encoded in the Co 2*p* region. However, first-row transition metal 2*p* core level spectra can exhibit complex line shapes arising from shake-up, plasmon loss, Coster-Kronig induced spectral broadening (51), and multiplet splitting associated with various core hole/VB localized state couplings (52, 53, 54) that can complicate fitting (46, 54, 55). These effects have an important influence on the overall spectral line shape, especially when different oxidation states and crystalline fields are present around the Co cations (46, 54, 55). Therefore, we have used the rigorous multiplet splitting approach developed by Biesinger et al. (54) to de-convolute Co $2p_{3/2}$ spectra. In this manner, it is possible to account for the possible different final states in the VB that arise due to VB/2*p* core hole coupling. Although this requires the fitting of a significant number of spectral components (46, 54, 55), the fitting components are highly constrained by their relative BE shifts, areal ratios, and widths, as reported by Biesinger et al. (54).

De-convolution of Co $2p_{3/2}$ core level spectra from the pristine biphasic CoO_x film (**Figure 2c**) under both vacuum and hydrated conditions confirms that the catalyst possesses a double layer structure comprising a $Co(OH)_2$ (Co^{2+}) overlayer on top of a Co_3O_4 mixed (Co^{2+}, Co^{3+}) oxide phase. This is in agreement with our prior findings (37), as well as from the multipeak fitting procedure performed on the O 1*s* core level, whose fine structure can be resolved by using three spectral components centered at different BE: Co-O bonds (BE = 530.2 eV), adsorbed OH (OH_{ads}, BE = 531.4 eV), and adsorbed H_2O (H_2O_{ads}, BE = 532.2 eV) (56). It is important to note that the BE values measured in this work are slightly higher – by approximately 0.4 eV – than those reported in literature for similar systems. This is due to recoil effects when momentum is transferred from the ejected photoelectron to the emitting atom. Recoil is present in all photoemission processes and the corresponding loss of photoelectron kinetic energy (ΔE_K) is given by $\Delta E_K = E_K (m_e/M)$, where E_K is the photoelectron kinetic energy, m_e is the electron rest mass, and *M* the emitting atom mass (49). Therefore, recoil effects are not negligible for high photoelectron kinetic energy and light elements (49, 57) and the energy difference observed here is a consequence of the larger photon energy used in the present work (4 keV) compared to typically used soft X-rays (< 2 keV).

A detailed analysis of the VB photoemission spectra from the biphasic coating is reported in **Figure 2d** for the cases of measurement under pristine, hydrated, and electrochemical conditions. The VB consists of three different regions, whose spectral features can be identified by their positions with respect to the Fermi level, which is defined as the zero of the binding energy scale. The first region, within the first 3 eV below the Fermi level, comprises the occupied states at the upper edge of the VB. These states are generated by low energy hybridizations of highly localized and strongly correlated Co 3*d* electronic states with O 2*p* levels (61). The states that fall in this region are mainly responsible for defining hole transport properties and chemical interactions, and thus the catalytic activity, of the material. The second region, between 3 and 7 eV below the Fermi level, is generated mainly by hybridization of O 2*p* orbitals, forming a relatively broad electronic band. Finally, beyond 8 eV below the Fermi level, hybridizations between O 2*p* valence orbitals from adsorbed and multilayer water on the WE surface contribute to the spectral intensity (58, 59, 60). The broad band at ~10.1 eV below the Fermi level arises from photoemission of the $1b_1$ molecular orbital of water (58, 59). The presence of such a spectral feature on the pristine sample measured at 10 Torr is a consequence of water adsorption on the WE surface due to the chamber environment. After the dip and pull procedure, the intensity of this component is enhanced. Under such conditions, a second spectral fingerprint, near 17.8 eV, is observed and can be assigned to photoemission from the $1b_2$ molecular orbital of liquid water (60).

Analysis of VB spectra obtained under pristine and hydrated conditions confirms the presence of both Co^{2+} and Co^{3+}, centered at 2.1 eV and 1.2 eV below the Fermi level, respectively. These two spectral features are due to the 3*d* band photoemission of octahedral Co^{2+} (from $Co(OH)_2$) and Co^{3+} (Co_3O_4 spinel structure), which leads to the $(t_{2g})^6$ and $(t_{2g})^5$ final states, respectively, that contribute to the valence band maximum (VBM) (56, 61). Tetrahedral Co^{2+} centers from Co_3O_4 give rise to $(e)^3(t_2)^3$ and $(e)^4(t_2)^2$ final states, which form a broad band at approximately 3.8 eV below the Fermi level.

Evolution of the biphasic catalyst surface structure as a function of the applied potential

In order to understand the evolution of the catalyst structure as a function of the applied electrochemical potential, we performed numerical simulations of the photoelectron intensity of the different spectral fitting components forming the measured Co $2p_{3/2}$ core level (see **Figure 2c**). The numerical simulations were performed using the "Simulation of Electron Spectra for Surface Analysis" (SESSA) software developed by Smekal, Werner, and Powell (62, 63). Owing to the conformal nature of the investigated systems, as reported in our previous work (37), continuous layer stacks given by "thickness equivalents" were used to represent the catalyst structure throughout the whole investigation as a function of the applied electrochemical potential. This approach, which is similar to that used in our recent study (48, 50), provides critical insights into changes of the layered catalyst structure, though quantitative thickness values must be taken as approximate and may be affected by material density and photoelectron inelastic mean free path (IMPF) differences in the different phases. Additional details of the approach can be found in the experimental section.

The results of spectral simulation and analysis are summarized in the bar chart of **Figure 3**. Under pristine conditions, the biphasic catalyst film comprises an approximately 18 Å thick interfacial Co_3O_4 spinel layer, on top of which is an approximately 22 Å thick $Co(OH)_2$ layer. This structure does not undergo significant changes under hydrated conditions. In contrast, measurement under electrochemical conditions results in significant changes to the catalytic film. When measured at U_{OCP}, following stabilization by running three CVs between the double layer region and the OER condition at 1900 mV vs. RHE, partial oxidative conversion of the $Co(OH)_2$ overlayer into CoO(OH) is observed. However, once the potential is held above the $Co^{3+} \rightarrow Co^{4+}$ transition (1713 mV vs. RHE), complete oxidative conversion of the di-hydroxide layer into the oxy-hydroxide is observed. This is also confirmed by analysis of the VB region (**Figure 2d**), where the relative spectral intensity from the Co^{+2} 3*d* band near 2.1 eV is reduced. Importantly, this feature is not entirely eliminated, which is consistent with the presence of the underlying Co_3O_4 layer, as also observed from analysis of the Co $2p_{3/2}$ region. These observations are in agreement with those reported by Weidler et al. on CoO_x prepared via chemical vapor deposition (CVD) (56) and characterized by *ex situ* XPS following galvanostatic electrochemical conditioning conducted at 10 mA cm^{-2}. However, it is noteworthy that our results show that the complete oxidative conversion occurs for electrochemical potentials below the OER operating conditions, i.e. within the so-called pre-catalytic range. As described in a previous report (48), this is an important property, since it shows that the overpotential for generating the phase supporting highest catalytic activity is lower than that of the oxygen evolution onset. In addition, it shows that highest activity oxygen evolution occurs on Co oxides only when CoO(OH) is present on the surface. Therefore, in order to decrease the OER overpotential, it may be essential to kinetically promote formation of this phase. As discussed below, the presence of $Co(OH)_2$ on the top surface of the starting material is found to serve this purpose and enhances catalytic activity relative to initially spinel Co_3O_4 surfaces. Moreover, it is important to highlight that the chronoamperometry data presented in **Figure 3** reveal that there is no significant change of the current density at fixed potentials, particularly under OER conditions. This supports the observation that the electrocatalytic activity of the film during the *operando* experiment was stable, and is consistent with our previous findings (37).

As shown in **Figure 2c** and represented in **Figure 3**, under sustained electrochemical bias in the pre-catalytic range, which is anodic of the $Co^{3+} \rightarrow Co^{4+}$ oxidation potential but cathodic of the onset for OER, not only does the $Co(OH)_2$ overlayer transform into the oxy-hydroxide phase, but a sub-nanometer domain of the underlying Co_3O_4 phase also undergoes a similar oxidative conversion. This finding confirms the previous *operando* XAS results reported by Bergmann et al. (31) that very thin surface layers of Co_3O_4 can be converted into $CoO_x(OH)_y$ under anodic bias. Critically, the thickness of the converted layer is significantly smaller than the total Co_3O_4 layer thickness, which enables a stable interface to the underlying silicon substrate.

Formation of the CoO(OH) phase is confirmed by the upward shift of the BE of the chemisorbed H_2O component in the O 1*s* core level region (**Figure 2a**), which moves from 532.2 eV to 532.6 eV when the adsorption takes place on the $Co(OH)_2$ and on the CoO(OH) structure, respectively. This phenomenon was also observed by Weidler and coworkers using *ex situ* methods (56). Although the detailed cause of such a shift remains partially unclear, it is possible to qualitatively understand this observation by taking into account the overall positive charge experienced by the Co^{3+} in the oxy-hydroxide phase. The interaction of water with these highly polarized metal centers could lead to a higher chemisorption energy, resulting in the observed upward shift of the corresponding spectral component.

More subtle changes are observed when the potential is swept from the pre-catalytic range to the OER catalytic range and held there (U = 1855 mV vs. RHE). As shown in **Figure 3**, the effective thickness of the $Co(OH)_2$ surface layer increases slightly as a consequence of additional transformation of underlying Co_3O_4. Nevertheless, a stable Co_3O_4 interfacial layer to the substrate, approximately 1 nm thick, is retained under sustained operation at this bias.

Importantly, under OER conditions, a new feature emerges on the low BE side of both Co $2p_{3/2}$ and O 1*s* core level spectra, as highlighted in green in **Figures 2a** and **c**. Experimental spectral shapes cannot be described without inclusion of these components and they are only observed under OER conditions. To the best of our knowledge, such features have not been previously reported. Here, we discuss the possible origins of these newly observed spectral components that arise as the catalyst drives the OER.

First, we consider the possibility of electronic decoupling of the outer surface region of the CoO(OH) layer from the conductive substrate. This effect could arise from electronic shielding of the outermost catalyst layer by intercalated ions in the oxy-hydroxide phase following transformation from $Co(OH)_2$ to CoO(OH). In this case, a potential offset will exist between the Fermi level of the sample and that in the electronically decoupled region, which will experience the potential drop within the electric double layer (EDL), whose thickness is approximately 2.2 nm (KOH 1.0 M, pH 13.8). Thus, both Co $2p_{3/2}$ and the corresponding reticular O 1*s* core levels would undergo a spectral shift toward lower BE due to the applied anodic potential. Such a decoupling effect has been observed from electrochemical measurements of layered oxyhydroxide OER catalysts on semiconductor substrates (64). On the other hand, it is important to note that ion intercalation and complete conversion of the system into the CoO(OH) phase occurs prior to reaching OER conditions. In particular, **Figures 2** and **3** show that transformation to CoO(OH) occurs at 1713 mV vs. RHE, which is cathodic of

the OER onset. Therefore, such an ion-induced electronic shielding and decoupling effect would be expected to take place at this potential as well, though be shifted by -0.15 eV according to the difference in applied potentials. However, we do not observe the low BE component on the Co $2p_{3/2}$ peak to emerge until the onset of OER, despite the fact that the effective thickness of CoO(OH) is nearly identical at applied electrochemical potentials of 1713 mV and 1855 mV vs. RHE. Furthermore, such an electronic decoupling should have a significant effect on the observed BE of O 1*s* from adsorbed H_2O, which is present near 532.6 eV, as described above. However, the position of this peak remains approximately constant, and its relative spectral weight is not measurably affected by bias condition. Given these factors, it is deemed unlikely that electronic shielding within the ultra-thin catalyst layer is the origin of the low BE features observed under OER conditions.

Second, we consider the possibility that electronic decoupling between regions of catalyst and the substrate may arise from physical delamination of CoO_x domains, which could occur due to the presence of mechanical strains during oxygen evolution. Such a mechanism of physical delamination and electronic decoupling is expected to be irreversible. In contrast, we find that cycling of the applied potential back to the pre-catalytic electrochemical potential range yields a reversible disappearance of the low binding energy Co 2*p* and O 1*s* spectral features, as shown in **Figures 2a** and **2c**. In addition, as described above, no significant change of the O 1*s* signal from adsorbed H_2O is observed. Therefore, we conclude that physical delamination and associated electronic decoupling of CoO_x domains under OER conditions does not contribute significantly to the observed spectral changes.

Third, we consider the possibility of corrosion and leaching of Co from the solid layer and into the electrolyte as an aquo complex. Solubilized Co aquo complexes would experience the potential shift between the WE and the solution. However, it is necessary to consider that concentrations of solutes below 100 mM in liquid phases are challenging to probe because of the XPS detection limit. While Co has a finite solubility, it is much below this value. Furthermore, we have previously analyzed electrolyte compositions following sustained operation of these CoO_x catalysts and found no evidence for appreciable corrosion and Co dissolution (37). Therefore, it is considered unlikely that solution phase Co species contribute to the observed photoemission spectrum. Furthermore, in both cases described above the BE shift between the low BE component and the main CoO(OH) spectral contribution (at 780.18 eV) should be less than or equal to 0.85 eV, corresponding to the applied electrochemical potential of 850 mV (vs. $Ag/AgCl/Cl^-_{(sat.)}$). On the other hand, the observed BE shift is significantly larger (1.12 eV). Moreover, an important fact to highlight is that the apparent decrease of the Co-O spectral component under operando conditions is due to an increase of the electrolyte layer thickness, and not because of a Co leaching into solution. As the applied electrochemical potential increases, the increase of the surface hydrophilicity (due to the oxidative conversion of the CoO_x catalytic layer) causes a thickening of the electrolyte layer, which then grows as the measurement proceeds. To determine the exact thickness of the liquid layer at the various investigated conditions, we have performed Monte Carlo simulations of the photoelectron intensity (using SESSA software (62, 63)) simulating the Co-O to LPW ratio for different liquid layer thicknesses, and comparing the results with the experimental ratio. The results are reported in **Figure S1a** and **b**, showing that the electrolyte layer thickness increases from about 19 to 30 nm between the start and end of the measurement. This increase of the liquid electrolyte thickness results in an apparent decrease of the H_2O_{ads} and OH_{ads} spectral components due to the exponential decay of the photoelectron intensity within the electrolyte layer (**Figure S1c**).

Fourth, and finally, we consider that the emergence of new spectral features could result from generation of highly oxidized Co^{4+} centers under OER conditions, as reported in the literature on the basis of electrochemical and infrared spectroscopic data (32, 37, 65, 66). Under sustained electrochemical water splitting conditions, the formation of two adjacent oxo-bridged Co^{3+} centers (Co^{3+}(OH)-O-Co^{3+}-OH) readily occurs at the catalyst surface. Subsequently, formation of Co^{4+} centers (Co^{4+}(=O)-O-Co^{3+}-OH) occurs via hole/proton hopping between Co^{3+} centers. Isolated Co^{4+} centers have been demonstrated to exhibit slow O_2 evolution kinetics (65). On the other hand, the increasing Co^{4+}=O density on the catalyst surface under OER conditions (controlled by the reaction rate determining step) leads to the creation of adjacent oxo-bridged Co^{4+} centers (Co^{4+}(=O)-O-Co^{4+}=O) where the concerted oxidation of water to molecular oxygen occurs with a fast turn-over-frequency (TOF > 3 s^{-1} (65)). At equilibrium conditions, a steady-state concentration of Co^{4+} is present on the electrode surface and can be detected with different spectroscopic methods (32). To the best of our knowledge, no photoelectron data of Co^{4+} species have yet been reported. Assignment of this feature to Co^{4+} is supported by its presence only under OER conditions and its disappearance as the potential is swept back into the pre-catalytic range.

As described above, the emergence of a new feature in the Co $2p_{3/2}$ region is consistently accompanied by the presence of a low BE component in the O 1s core region; this component is located at 529.22 eV compared to the main O^{2-} component (Co-O) centered at 530.19. This feature appears to be correlated with the presence of the lower BE feature in the Co $2p_{3/2}$ region and is only observed under OER conditions (see **Figure 2a**). Pfeiffer *et al*. recently showed evidence of peroxide species (O^-) on IrO_x catalyst under OER conditions using soft X-ray APXPS, which revealed an O 1*s* component in the same spectral range (67). However, for the case of CoO_x, the presence of a peroxide species implies binding to Co^{3+} (65, 66), which does not account for the low BE component observed on the Co 2*p* spectrum under OER conditions. An alternative explanation for emergence of a low binding energy component to the O 1s signal under OER conditions comes from the fact that Co^{4+}=O is considered to be in electronic resonance with Co^{3+}-O● (65). Thus, this signal could be directly linked to the active site. Similarly, it could also arise from reticular oxygen (O^{2-}) embedded in highly oxidized structures (46, 55, 68, 69, 70), such as the oxo-bridged Co^{4+} centers Co^{4+}(=O)-O-Co^{4+}=O described above. While either of these spectral assignments is physically reasonable based on the composition of the film and prior mechanistic studies, it is not currently possible to discriminate between these spectral components.

Previously, Weidler et al. also observed an additional small intensity O 1s component at low BE from a CoO_x catalyst surface, *ex situ* after exposure to highly oxidizing electrochemical conditions, but they did not attribute it to any related Co chemistry (56). Since electronic decoupling or Co leaching can be observed only while running the electrochemical measurements, this prior finding supports our hypothesis that the observed BE shift is indeed correlated to a chemical shift of a new Co-based species developing on the catalyst surface under sustained OER conditions.

As can be seen by comparing **Figure 2a** and **2c**, the relative contribution of the low BE component is higher in the Co $2p_{3/2}$ spectrum than in the corresponding O 1*s* one. This could be explained by a lower atomic concentration of oxygen moieties than Co moieties contributing to the core level signals, as given by atomic scale differences in the highly oxidized sites. Also, it is important to consider the different probed volume achieved with Co $2p_{3/2}$ and O 1*s* core level photoemission. Since the photon energy was kept constant at 4.0 keV throughout the whole APXPS experiment, Co $2p_{3/2}$ (KE = 3.22 keV) and O 1*s* (KE = 3.47 keV) spectra provide different surface sensitivities due to the larger kinetic energies of photoelectrons ejected from the O 1*s* level. The corresponding inelastic mean free paths (λ_e) of photoelectrons propagating through the layered Co_3O_4/CoO(OH) system created under OER conditions (**Figure 3**) corresponds to 44.1 Å for the Co$2p_{3/2}$ and 49.2 Å for the O 1*s* core level. Since the probed volume, from which 95% of photoelectrons are emitted, is equal to $3\lambda_e$, the differential probed volume is therefore equal to 15.3 Å, with the Co spectrum exhibiting a greater surface sensitivity. A similar argument can be invoked to explain the fact that no clear changes are observed in the corresponding VB spectra under OER conditions (**Figure 2d**), since for VB photoemission at the Fermi level (KE ~ 4.0 keV) λ_e is equal to 54.8 Å.

Following measurement under OER conditions, the reversibility of the surface transformation observed by APXPS was investigated by analyzing the evolution of the core level and VB spectra at 1604 mV vs. RHE, which is the potential associated with the $Co^{4+} \rightarrow Co^{3+}$ transition, as well as at the resting OCP. As shown in **Figure 2c** and **Figure 3**, while conversion of the CoO(OH) back to $Co(OH)_2$ is observed, the reaction is not entirely reversible. The result is that only the topmost layers undergo reductive conversion and significant remnant CoO(OH) is retained under the surface. We note that prior studies have concluded that the $Co(OH)_2$ to CoO(OH) transition is irreversible (71). However, that work was based on electrochemical evaluation of much thicker layers, where the presence of a reversibly transformed surface $Co(OH)_2$ layer would not be readily detected. Therefore, our findings are consistent with those of prior works and suggest that the surface hydroxide may serve to suppress transformations of the underlying oxyhydroxide phase.

Comparison between the biphasic and monophasic catalysts

To provide additional insight into the role of the $Co(OH)_2$ surface layer on catalytic activity, we compared the electrochemical bias-dependent APXPS of the biphasic coating with that of a monophasic layer composed of pure spinel Co_3O_4. As described previously, this layer was obtained by PE-ALD onto p^+-Si at a substrate temperature of 300 °C, compared to 100 °C used to create the biphasic coating (37). Consistent with prior results, electrochemical characterization of the monophasic film beyond the pre-catalytic region (i.e. 1918 mV vs. RHE) reveals lower catalytic activity for oxygen evolution than the biphasic coating (**Figure 4a**) (37).

Figure 4b shows a comparison of Co $2p_{3/2}$ core level spectra obtained via *operando* APXPS on the monophasic and biphasic CoO_x films at U_{OCP} and under OER conditions. Regarding the monophasic catalyst, it can be seen that only a small fraction of the surface undergoes a partial reductive conversion to a $Co(OH)_2$ phase, consistent with prior findings for Co_3O_4 spinel. At more anodic potentials, where OER occurs, a sub-nanometer layer, approximately 5 Å thick, of CoO(OH) forms. These results are summarized in **Figure 4c**, which reports the structure of the monophasic and biphasic systems under pristine and catalytic conditions. The results provided by *operando* APXPS explain the observed electrochemical *J-E* characteristics from the films (**Figure 4a**). In addition to the lower catalytic activity of the monophasic film, much weaker redox activity in the pre-catalytic range is observed. This finding is consistent with largely surface site-confined catalysis on the more chemically inert Co_3O_4 spinel. In contrast, the higher current densities measured from the biphasic material, in both the pre-catalytic and OER regimes, indicate higher overall redox activity for conversion from the $Co(OH)_2$ to the CoO(OH) phase, as well as a higher concentration of catalytically active sites that extend into the volume below the surface (selvedge region).

Unlike for the case of the biphasic catalyst coating, no low BE features in either the Co $2p_{3/2}$ or the O 1s region are observed for the case of the monophasic coating under OER conditions. The lack of such spectral components from the Co_3O_4 coating is consistent with the notion that they are related to the presence of Co^{4+} and reticular O^{2-} sites associated with catalytic processes within CoO(OH). Indeed, under OER conditions, the CoO(OH) layer thickness is six times thicker for the biphasic film compared to the monophasic film, which would preclude their detection in the latter case within the sensitivity of the present APXPS measurements.

These findings highlight the value of tailoring biphasic (photo)electrocatalysts (37, 72), having a chemically and structurally labile phase, such as $Co(OH)_2$ (37) or CoO (72), on top of a compact nanocrystalline Co_3O_4 spinel layer. Such labile phase atop the chemically inert Co_3O_4 is important for enhancing the catalytic activity of the overall assembly by promoting formation of Co^{4+} sites that participate in the catalytic cycle (37, 72), while also providing stable interfaces to potentially sensitive substrates (72). Furthermore, the presented results shed light on an emerging picture of OER catalysis, whereby increasing concentrations of active sites within the bulk can contribute to higher overall activity per geometric area.

Conclusion

In conclusion, the results of our *operando* APXPS study shed light on the nature of electrochemical transformations of cobalt oxides, as well as the crucial role of the $Co(OH)_2$ to CoO(OH) transition on enabling OER electrocatalytic activity. The coupling of experimental photoelectron data with numerical simulations of core region line shapes and photoelectron intensity attenuation allowed us to track the evolution of structure of an advanced biphasic cobalt oxide coating formed via PE-ALD. In addition to revealing electrochemical transformations, these measurements revealed the emergence of new spectral contributions at low binding energies within both the Co 2p and O 1s core level regions. These features were only observed when both CoO(OH) was present and the applied electrochemical bias was sufficient to drive the oxygen evolution reaction, as revealed by analysis of APXPS spectra obtained under different bias conditions. Comparison of this biphasic catalyst with a monophasic Co_3O_4 spinel coating formed using the same method but at higher deposition temperature, provided additional support for this interpretation.

The electrochemical phase behavior of the biphasic cobalt oxide coating was found to promote desirable characteristics for integration with chemically sensitive substrates, such as

semiconductor light absorbers. In particular, the relative phase stability of Co_3O_4 enables a durable substrate/catalyst interface, while facile chemical transformation of $Co(OH)_2$ to CoO(OH) layered structure promotes high catalytic activity. Beyond this specific cobalt oxide system, the experimental strategy presented in this work can be successfully extended for the study of different materials and catalytic reactions. Indeed, we have demonstrated that the *operando* APXPS technique can be efficiently used for studying complex electrocatalytic reactions that play a crucial role in sustainable energy conversion.

Methods

Deposition of CoO_x by plasma-enhanced atomic layer deposition (PE-ALD)

As a conductive substrate, p^+-Si (B-doped, resistivity of 0.001-0.005 Ω cm^{-1}) wafers were used. The CoO_x catalyst layers were deposited using a remote plasma-enhanced atomic layer deposition (Oxford FLexAl) (PE-ALD) process at target temperatures ranging from 100 °C to 300 °C. The cobalt precursor was cobaltocene ($CoCp_2$) (98% Strem Chemicals) and a remote oxygen plasma served as the oxidant (37). The precursor lines, carrier gas lines, and the reactor walls were kept at 120 °C. The $CoCp_2$ precursor bubbler was heated to 80 °C and bubbled with 200 sccm (standard cubic centimetre per minute) of high purity Ar gas during the precursor exposure half cycles. Oxygen gas flow was held constant at 60 sccm throughout the deposition process. The cobalt precursor exposure half cycle consisted of 5 s $CoCp_2$ dosing and 5 s purging (37). The remote oxygen plasma half cycle consisted of 1 s pre-plasma treatment, 5 s plasma exposure, and 15 s purging. The plasma power was 300 W and was applied for 5 s during the oxygen plasma half cycle (37). The deposition chamber was maintained at 15 mTorr at all times. The film thicknesses were measured using UVISEL spectroscopic ellipsometer (Horiba Jobin Yvon). The average growth rate was ~0.5 Å/cycle (37). We note that the high stability of the PE-ALD CoO_x films on planar Si substrates is important for allowing *operando* APXPS measurements, which require relatively long times of sustained exposure to electrolyte and electrochemical bias. Likewise, the high homogeneity of the films allows for interpretation of photoemission data averaged over the spot size (300 μm).

Beamline 9.3.1 and APXPS experimental details

Experiments were performed at Beamline 9.3.1 at the Advanced Light Source (ALS, Lawrence Berkeley National Laboratory), which is equipped with a bending magnet and a Si (111) double crystal monochromator (DCM) spanning the photon energy range between 2.0 keV and 8.0 keV (*i.e.*, the "tender" X-ray range) (39). The analyzer (R4000 HiPP-2, Scienta) pass energy was set to 200 eV and data were collected using 100 meV steps with a dwell time of 300 ms at each energy. Under these conditions, the total resolution (source and analyzer) was equal to 320 meV at room temperature. The measurements were taken using a photon energy of 4.0 keV at room temperature and in normal emission (NE), at a pressure in the experimental chamber ranging from 15 to 18 Torr (see following section), while the detection stage in the analyser was maintained under high vacuum conditions (~2×10^{-7} Torr) by differential pumping. The calibration of the binding energy (BE) scale was carried out using the Au 4f photoelectron peak ($4f_{7/2}$ BE = 84.0 eV) and the Fermi edge as reference, measured from a clean polycrystalline Au surface.

A Doniach-Šunjić line shape was used for fitting the Au 4*f* photoelectron peak, whereas a symmetrical Voigt function (G/L ratio ranging from 85/15 to 75/25) was used to fit O 1*s* and valence band (VB) photoelectron peaks, as well as to simulate and de-convolute the Co $2p_{3/2}$ photoelectron spectra, which was accomplished via the mixed state multiplet splitting approach (54) (after Shirley background subtraction). During the fitting procedure, the Shirley background was optimized together with the spectral components, thereby increasing the precision and reliability of the fitting procedure (73, 74, 75). The χ^2 minimization was ensured by the use of a nonlinear least squares routine, with increased stability over simplex minimization (74).

Electrochemical measurements and "Dip and Pull" method

All chemicals used in this study were high purity reagents and used as-received. MilliQ water (DI, ρ=18.2 MΩ·cm) was used as solvent, while KOH (99.99%, Aldrich) was used as supporting electrolyte. The electrochemical cell was arranged in the three-electrode configuration, with a polycrystalline Pt foil (Aldrich) used as the counter electrode (CE). Prior to cell assembly, the CE was polished to a mirror finish with silicon carbide papers of decreasing grain size (Struers, grit: 2400 and 4000) and then cleaned by two cycles of ultrasonic treatment in a mixture of MilliQ water/ethanol (Aldrich, 1:1) for 10 min. A third ultrasonic cleaning was then conducted in pure MilliQ water for 15 min, followed by thorough rinsing and drying in a N_2 stream. For the reference electrode (RE), a miniaturized leakless Ag/AgCl/$Cl^-_{(sat)}$ electrode (ET072-1, eDAQ) was used ($U^{\emptyset}_{\mathrm{Ag/AgCl\,(sat.)}} = 0.199$ V vs. normal hydrogen electrode, NHE, at 298 K). The resistance of the electrolyte in the fully-immersed electrode configuration (R = 1.8 Ω) and after the dip and pull procedure (R = 15.0 Ω) was measured with electrochemical impedance spectroscopy (EIS) (48). The resistance value obtained after the dip and pull procedure was used for the *iR* drop post-correction of the applied electrochemical potentials. Unless otherwise stated, the potentials reported in this work are referred to the reversible hydrogen electrode (RHE), which is related to the Ag/AgCl/$Cl^-_{(sat)}$ electrode and the electrolyte pH by the following relation:

$$U_{\text{vs. RHE}} = U_{\text{vs. Ag/AgCl (sat.)}} + U^{\emptyset}_{\mathrm{Ag/AgCl\,(sat.)}} + 0.0591 \cdot \mathrm{pH}$$

The investigated materials, CoO_x-coated p^+-Si wafers, were configured as the working electrodes (WE) and were thoroughly rinsed using pure MilliQ water and drying in a N_2 stream immediately prior to loading the cell.

The three electrodes were connected to a Biologic SP 300 potentiostat/galvanostat, which was employed for the *operando* electrochemical measurements. All cyclic voltammograms (CV) reported in this work were acquired at room temperature (~298 K) and at a potential scan rate of 20 mV s^{-1}. Current densities were determined by normalizing measured currents to the geometrical areas of the electrodes exposed to the electrolyte medium.

Before its introduction into the experimental chamber, the electrolyte (KOH 1.0 M aqueous solution) was outgassed for at least 30 min at low pressure (approximately 10 Torr) in a dedicated off-line chamber. Then, the manipulator and the outgassed electrolyte were placed into the experimental chamber and the pressure was carefully reduced by pumping down to the water vapour pressure (between 15 and 20 Torr, at room temperature). Finally, the "dip and pull" procedure

was carried out, as described previously, in order to obtain a stable and conductive nanometer-thick electrolyte layer on the WE surface (39, 42-44, 46, 48).

Numerical simulations of the photoelectron intensity

The numerical simulations of the photoelectron intensity were developed using the Simulation of Electron Spectra for Surface Analysis (SESSA) software. Technical details about this tool can be found in ref. (62) and (63). From observations already reported in literature about the oxidic surface structure of monophasic and biphasic catalysts (37), the simulations were built adopting a conformal layer-by-layer structure "buried" underneath an electrolyte (KOH 1.0 M) film characterized by an average thickness of 18 nm.
The simulations were performed using net and well-defined layer/layer interfaces. This approximates the real configuration, where gradients and mixed regions may exist at layer/layer interfaces. However, the spatial extension of such regions are typically of about 1-2 nm, a dimension that is typically difficult to access and discriminate with tender X-rays. Furthermore, previously reported atomic force micrographs revealed the surfaces of such CoO_x/Si electrodes to have root mean square (RMS) roughnesses of <3 Å and transmission electron micrographs showed abrupt interfaces. Therefore, the approximation used here is reasonable for analysis of the APXPS data.
Similarly to what we previously performed on Pt electrodes under OER conditions (48), for a chosen model, we have investigated different spatial localization of the oxidic phases. The model that fitted the experimental data best was determined by using a chi-square (χ^2) statistical test. The quantities used for its evaluation were the Co_3O_4 (R_1), $Co(OH)_2$ (R_2), and CoO(OH) (R_3) components, which were determined experimentally through the multipeak fitting procedure (54) of the Co $2p_{3/2}$ photoelectron peak (EXP) and from the numerical simulations (SIM). Therefore:

$$\chi^2 = \sum_{i=1,2,3}^{\alpha,\beta} \left(R_i^{\mathrm{EXP}} - R_i^{\mathrm{SIM}}\right)^2 ,$$

where α and β indicates a particular model and its configuration (equivalent thickness of the constituent layers).
For final evaluation of model/configuration, the space of parameters was explored using a variational principle: for each model, the minimum value of the χ^2 was achieved by properly adjusting the layer thickness of the different oxide layers. This procedure allows determination of both the structure and the corresponding configuration (layer thicknesses) that best match with the experimental results. However, we note that this approach assumes similar attenuation lengths in each phase. The absolute thickness values should be regarded as estimates and the major outcome of the simulations is to give the spatial localizations of the different Co chemistries in the pristine catalyst and under *operando* electrochemical conditions (48). Improved quantification could be achieved in the future using angle-resolved XPS, but is outside the scope of this report.

ASSOCIATED CONTENT

Supporting Information

Monte Carlo simulations of photoelectron intensities and intensity ratios as a function of liquid electrolyte thickness, electrolyte layer thicknesses as a function of APXPS measurement condition. This material is available free of charge via the Internet at http://pubs.acs.org.

AUTHOR INFORMATION

Correspondence to: M. Favaro (marco.favaro@helmholtz-berlin.de), J. Yano (jyano@lbl.gov) and I. D. Sharp (idsharp@lbl.gov).

Present address

[‡]Helmholtz-Zentrum Berlin für Materialien und Energie GmbH, Institute for Solar Fuels, Hahn-Meitner-Platz 1, D-14109 Berlin, Germany.

Author contributions

The manuscript was written through contributions of all authors. M.F. and I.D.S. planned the experiments. M.F. executed the experiments, evaluated the data and drafted the manuscript. J. Y. and I.D.S. prepared the samples and helped with data acquisition. S.N., E.M. and F.M.T. helped with data acquisition. F.M.T., J. Yano, I.D.S. and E.J.C. gave general advice and actively participated in drafting the manuscript.
All authors have given approval to the final version of the manuscript.

Competing financial interests

The authors declare no competing financial interests.

ACKNOWLEDGMENT

This material is based upon work performed by the Joint Center for Artificial Photosynthesis, a DOE Energy Innovation Hub, supported through the Office of Science of the U.S. Department of Energy under Award Number DE-SC0004993. Experiments were performed at the Advanced Light Source, which is supported by the Director, Office of Science, Office of Basic Energy Sciences, of the U.S. Department of Energy under Contract No. DE-AC02-05CH11231.

Figures

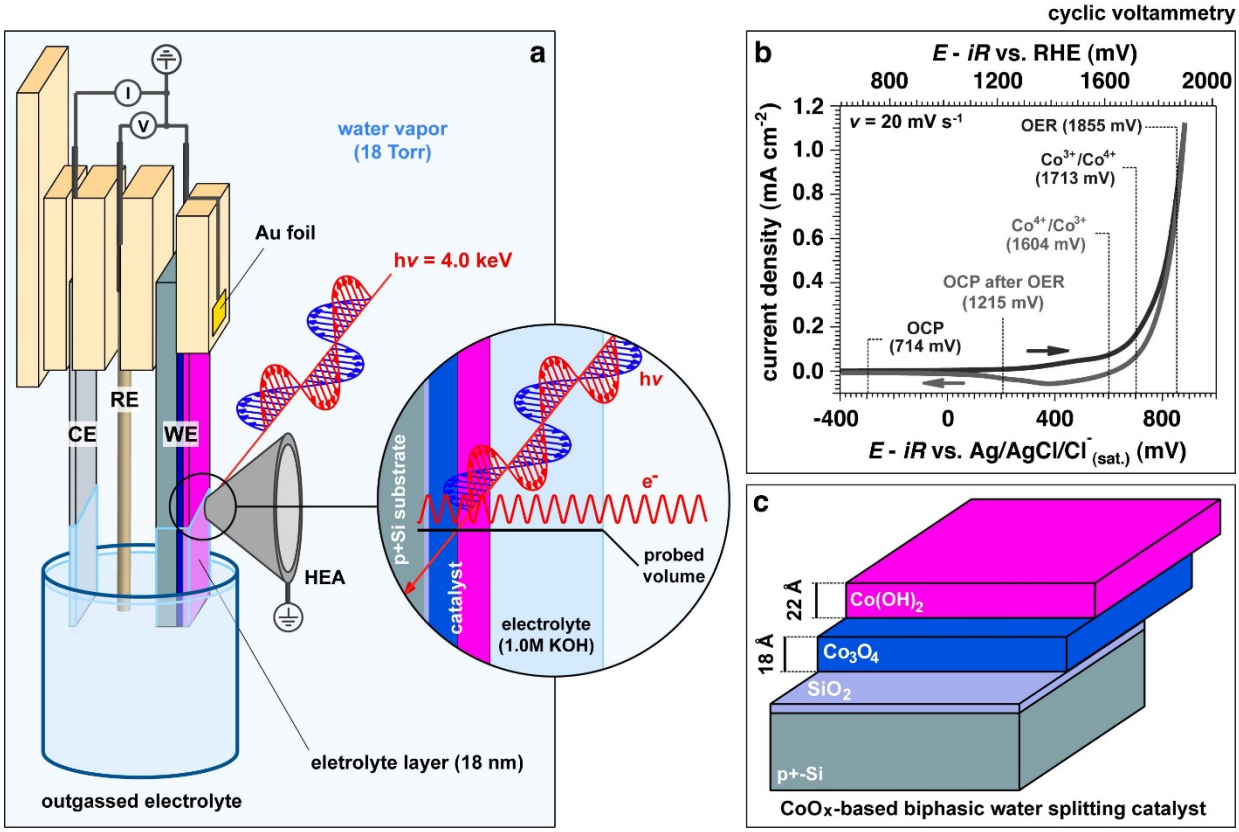

Figure 1. Three electrode electrochemical setup used for the *operando* APXPS experiment. (a) Schematic illustration of the experimental configuration used for *operando* electrochemical APXPS. CE: counter electrode; RE: reference electrode; WE: working electrode; HEA: hemispherical electron analyzer; (b) The cyclic voltammogram (CV) for the biphasic CoO_x layer, deposited via plasma-enhanced atomic layer deposition (PE-ALD) at a substrate temperature of 100° C, was acquired at T~298K at a scan rate of 20 mV s^{-1} and in a 1.0 M KOH aqueous solution (pH 13.8) in the analysis chamber with a water pressure equal to 18 Torr (OCP: open circuit potential; OER: oxygen evolution reaction); (c) Schematic illustration of the biphasic pristine CoO_x coating, comprising a disordered $Co(OH)_2$ phase, nanocrystalline spinel Co_3O_4, and SiO_2 on top of a p^+-Si substrate.

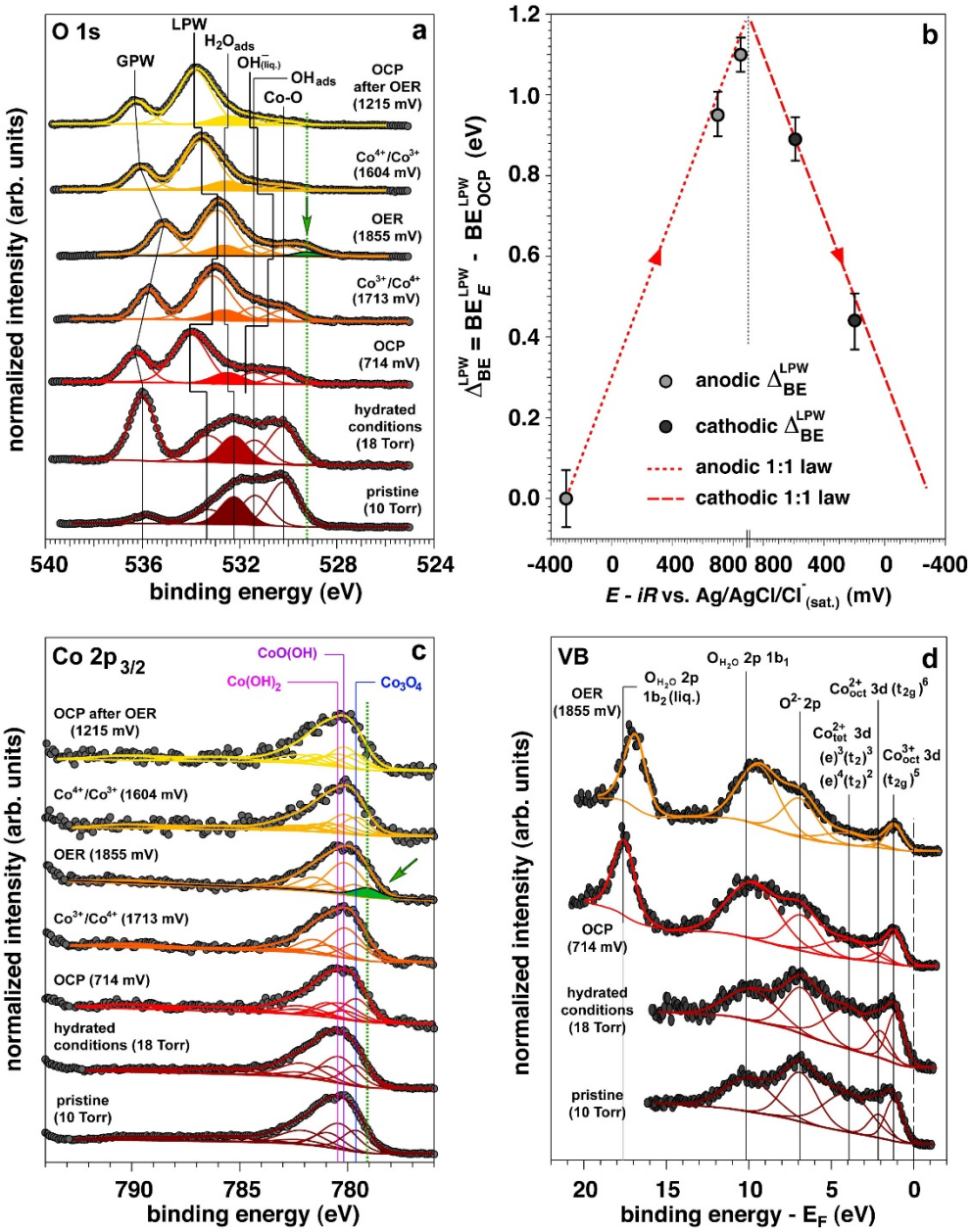

Figure 2. *Operando* ambient pressure X-ray photoelectron spectroscopy (APXPS) of the biphasic CoO_x catalyst. (a) *Operando* APXPS evolution of O 1*s* photoelectron peak (de-convoluted into chemically shifted spectral components) at hydrated conditions (18 Torr water vapor) and as a function of the applied potential; (b) O 1s LPW BE shift (Δ_{BE}^{LPW}) as a function of the applied electrochemical potential *U*. The dotted lines represent the linear dispersion of the O 1*s* LPW component with the applied potential, accordingly to the relation: $BE_{electrolyte} = BE_0 - eU$. The error bars were determined via repeated measurements and fitting of the O 1*s* photoelectron spectrum, propagated with the experimental spectral resolution (see Methods); (c, d) Co $2p_{3/2}$ and valence band (VB) (both de-convoluted into chemically shifted spectral components) acquired under hydrated conditions (18 torr water vapor) and as a function of the applied electrochemical potential, respectively (GPW: gas phase water; OCP: open circuit potential, OER: oxygen evolution potential, BE: binding energy). For figures a and c, the green-shadowed component at low BE, whose nature is explained in the text and assigned to Co^{4+}, is observable only at OER potentials. The reported electrochemical potentials are referred to the reversible hydrogen electrode (RHE).

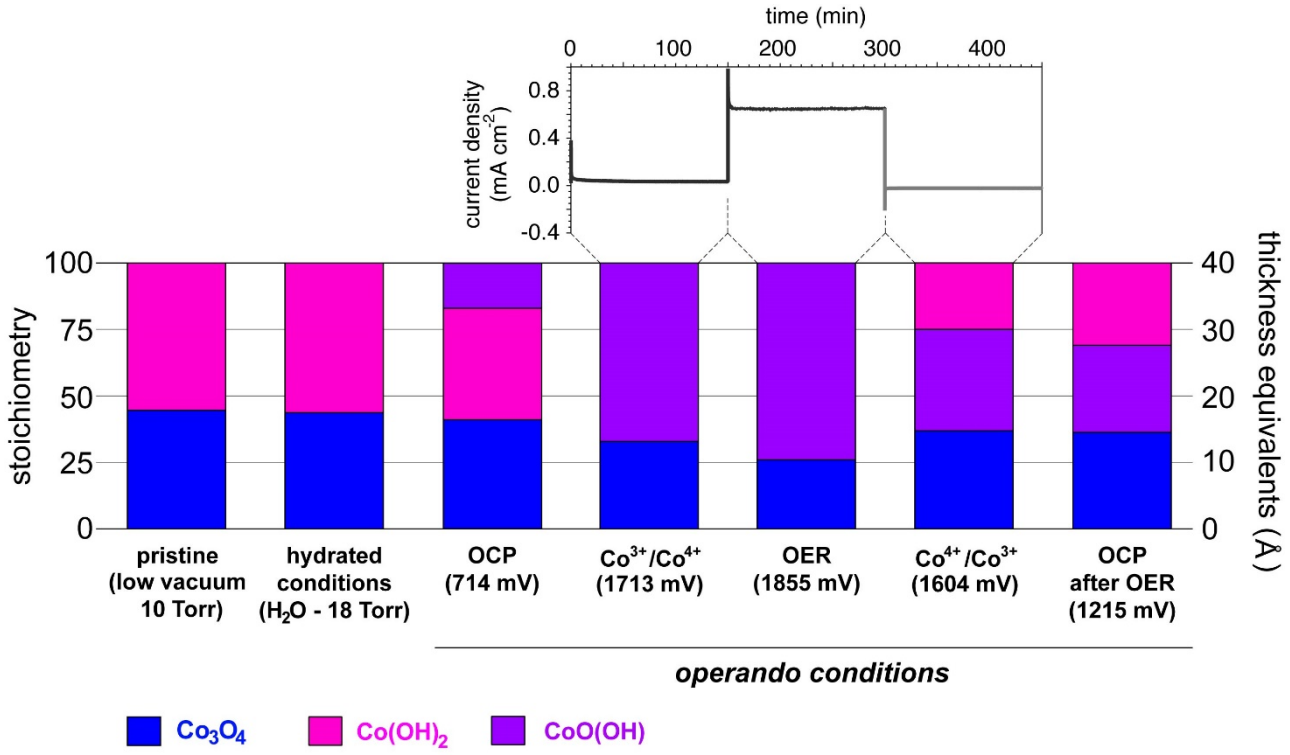

Figure 3. Evolution of the surface stoichiometry and structure of the biphasic catalyst as a function of the applied potential. The coupling between the *operando* Tender X-ray APXPS data and numerical simulations of the Co $2p_{3/2}$ photoelectron intensity attenuation (48, 62, 63) allows to determine the evolution of the catalyst surface and sub-surface chemistry and structure as a function of the applied potential across the polarization curve. Note that the stoichiometry was determined directly from the fitting procedure performed on the experimental Co $2p_{3/2}$ data. The thickness values are provided in "thickness equivalents" as the APXPS gives average information over a surface region of 300 μm in diameter (OCP: open circuit potential; OER: oxygen evolution reaction; OX: oxidative conversion; RED: reductive conversion). The reported electrochemical potentials are referred to the reversible hydrogen electrode (RHE).

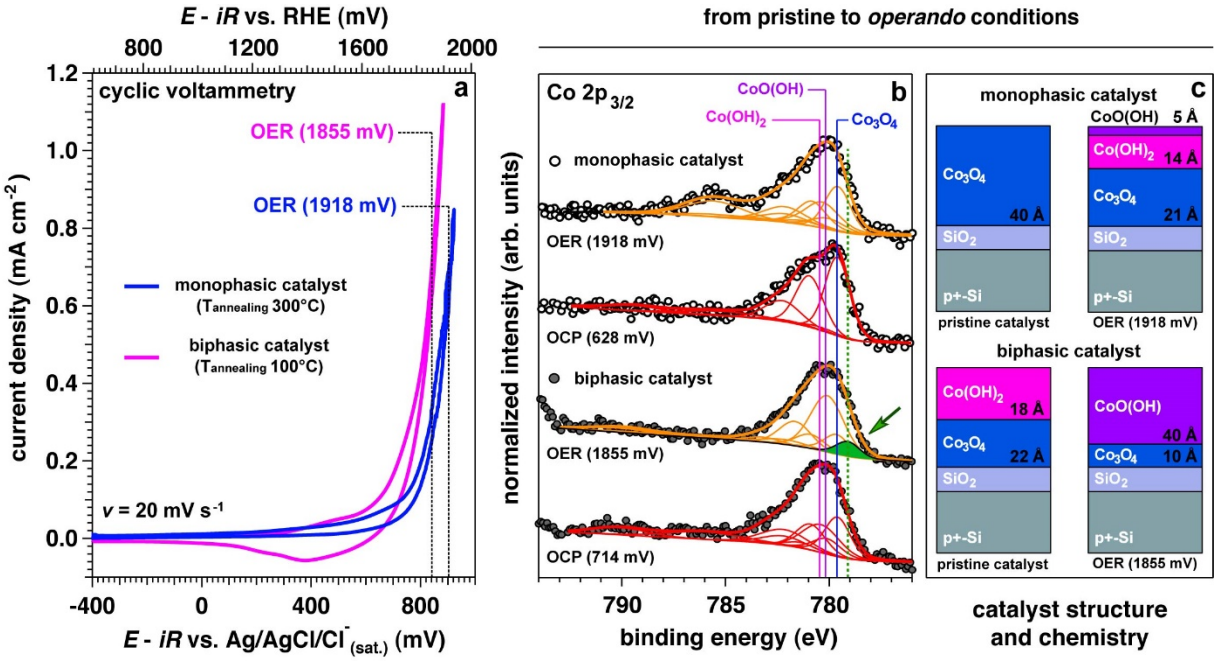

Figure 4. Comparison between monophasic and biphasic CoO_x catalysts. (a) Cyclic voltammetries (CV) for the 100° C- and 300° C-annealed CoO_x systems (biphasic and monophasic catalyst, respectively) (the CVs have been acquired at T~298K at a scan rate of 20 mV s^{-1} and in a KOH 1.0 M aqueous solution (pH 13.8), at water pressure in the chamber equal to 18 Torr); (b) Co $2p_{3/2}$ APXPS core levels acquired at the open circuit potential (OCP) and under oxygen evolution reaction (OER) conditions for two different CoO_x catalysts (the green-shadowed component at low BE, whose nature is explained in the text and assigned to Co^{4+}, is observable only at OER potentials); (c) chemical composition and sub-surface structure for the monophasic and biphasic catalysts, passing from pristine to OER conditions. Note that the chemical composition was determined from the fitting procedure performed on the experimental Co $2p_{3/2}$ data reported in b. The thickness values (determined from the numerical simulations of the photoelectron intensity attenuation of the different Co spectral components) are provided in "thickness equivalents" as the APXPS gives average information over a surface region of 300 μm in diameter. The reported electrochemical potentials are referred to the reversible hydrogen electrode (RHE).

References

(1) Obama, B. *Science* **2017**, 355, 126.

(2) Gust, D.; Moore, T. A.; Moore, A. L. *Acc. Chem. Res.* **2001** ,34, 40.

(3) Lewis, N. S.; Nocera, D. G. *Proc. Natl. Acad. Sci.* **2006**, 103, 15729.

(4) Kamat, P. V. *J. Phys. Chem. C* **2007**, 111, 2834.

(5) Tachibana, Y.; Vayssieres, L.; Durrant, J. R. *Nat. Photon.* **2012** ,6, 511.

(6) Zhang, P.; Wang, T.; Chang, X.; Gong, J. *Acc. Chem. Res.* **2016**, 49, 911.

(7) Ager, J. W. *Solar to Chemical Energy Conversion*. **2016**, 32, 249.

(8) Walter, M. G.; Warren, E. L.; McKone, J. R.; Boettcher, S. W.; Mi, Q.; Santori, E. A.; Lewis, N. S. *Chem. Rev.* **2010**, 110, 6446.

(9) Abdi, F. F.; Han, L.; Smets, A. H. M.; Zeman, M.; Dam, B.; van de Krol, R. *Nat. Commun.* **2013**, 4, 2195.

(10) Sun, J.; Zhong, D. K.; Gamelin, D. R. *Energy Environ. Sci.* **2010**, 3, 1252.

(11) Koza, J. A.; He, Z.; Miller, A. S.; Switzer, J. A. *Chem. Mater.* **2012**, 24, 3567.

(12) Trotochaud, L.; Ranney, J. K.; Williams, K. N.; Boettcher, S. W. *J. Am. Chem. Soc.* **2012**, 134, 17253.

(13) Hisatomi, T.; Kubota, J.; Domen, K. *Chem. Soc. Rev.* **2014**, 43, 7520.

(14) Haber, J. A.; Xiang, C.; Guevarra, D.; Jung, S.; Jin, J.; Gregoire, J. M. *Chem. Electro. Chem.* **2014**, 1, 524.

(15) Deng, X.; Tüysüz, H. *ACS Catalysis* **2014**, 4, 3701.

(16) Yang, J; Walczak, K.; Anzenberg, E.; Toma, F. M.; Yuan, G.; Beeman, J. et al. *J. Am. Chem. Soc.* **2014**, 136, 6191.

(17) Haber, J. A.; Anzenburg, E.; Yano, J.; Kisielowski, C.; Gregoire, J. M. *Adv. Energy Mater.* **2015**, 1, 1402307.

(18) Gerken, J. B.; Jamie J. G. M.; Chen, Y. C.; Rigsby, M. L.; Casey, W. H.; Britt, R. D.; Stahl, S.S. *J. Am. Chem. Soc.* **2011**, 133, 4625.

(19) Dau, H.; Limberg, C.; Reier, T.; Risch, M.; Roggan, S.; Strasser, P. *Chem. Cat. Chem.* **2010**, 2, 724.

(20) Farrow, C. L.; Bediako, D. K.; Surendranath, Y.; Nocera, D. G.; Billinge, S. J. L. *J. Am. Chem. Soc.* **2013**, 135, 6403.

(21) Mattioli, G.; Giannozzi, P.; Amore Bonapasta, A.; Guidoni, L. *J. Am. Chem. Soc.* **2013**, 135, 15353.

(22) Bediako, D. K.; Costentin, C.; Jones, E. C.; Nocera, D. G.; Savéant, J.-M. *J. Am. Chem. Soc.* **2013**, 135, 10492.

(23) García-Mota, M.; Bajdich, M.; Viswanathan, V.; Vojvodic, A.; Bell, A. T.; Nørskov, J. K. *J. Phys. Chem. C* **2012**, 116, 21077.

(24) Bajdich, M.; García-Mota, M.; Vojvodic, A.; Nørskov, J. K.; Bell, A. T. *J. Am. Chem. Soc.* **2013**, 135, 13521.

(25) Friebel, D.; Bajdich, M.; Yeo, B. S.; Louie, M. W.; Miller, D. J.; Sanchez Casalongue, H.; Mbuga, F.; Weng, T.-C.; Nordlund, D.; Sokaras, D.; Alonso-Mori, R.; Bell, A. T.; Nilsson, A. *Phys. Chem. Chem. Phys.* **2013**, 15, 17460.

(26) Li, X.; Siegbahn, P. E. M. *J. Am. Chem. Soc.* **2013**, 135, 13804.

(27) Kanan, M. W.; Yano, J.; Surendranath, Y.; Dincă, M.; Yachandra V. K.; Nocera, D. G. *J. Am. Chem. Soc.* **2010**, 132, 13692.

(28) Menezes, P. W.; Indra, A.; Bergmann, A.; Chernev, P.; Walter, C.; Dau, H.; Strasser, P.; Driess, M. *J. Mater. Chem. A* **2016**, 4, 10014.

(29) Sanchez Casalongue, H. G.; Ling Ng, M.; Kaya, S.; Friebel, D.; Ogasawara, H.; Nilsson, A. *Angew. Chem. Int. Ed.* **2014**, 53, 7169.

(30) González-Flores, D.; Sánchez, I.; Zaharieva, I.; Klingan, K.; Heidkamp, J.; Chernev, P. et al. *Angew. Chem. Int. Ed.* **2015**, 54, 2472.

(31) Bergmann, A.; Martinez-Moreno, E.; Teschner, D.; Chernev, P.; Gliech, M.; Ferreira de Araújo, J. et al. *Nat. Commun.* **2015**, 6, 8625.

(32) Risch, M.; Ringleb, F.; Kohlhoff, M.; Bogdanoff, P.; Chernev, P.; Zaharieva, I.; Holger, D. *Energy Environ. Sci.* **2015**, 8, 661.

(33) McAlpin, J. G.; Surendranath, Y.; Dincă, M.; Stich, T. A.; Stoian, S. A.; Casey, W. H. et al. *J. Am. Chem. Soc.* **2010**, 132, 6882.

(34) Du, P.; Kokhan, O.; Chapman, K. W.; Chupas, P. J.; Tiede, D. M. *J. Am. Chem. Soc.* **2012**, 134, 11096.

(35) Indra, A.; Menezes, P. W.; Sahraie, N. R.; Bergmann, A.; Das, C.; Tallarida, M. et al. *J. Am. Chem. Soc.* **2014**, 136, 17530.

(36) Klingan, K.; Ringleb, F.; Zaharieva, I.; Heidkamp, J.; Chernev, P.; Gonzalez-Flores, D. et al. *Chem. Sus. Chem.* **2014**, 7, 1301.

(37) Yang, J.; Cooper, J. K.; Toma, F. M.; Walczak, K. A.; Favaro, M.; Beeman, J. W.; et al. *Nat. Mater.* **2017**, 16, 335.

(38) Arrigo, R.; Hävecker, M.; Schuster, M. E.; Ranjan, C.; Stotz, E.; Knop-Gericke A.; Schlögl, R. *Angew. Chem. Int. Ed.* **2013**, 52, 11660.

(39) Axnanda, S.; Crumlin, E. J.; Mao, B.; Rani, S.; Chang, R.; Karlssom, P. G.; Edwards, M. O. M.; Lundqvist, M.; Moberg, R.; Ross, P. N.; Hussain, Z.; Liu, Z. *Sci. Rep.* **2015**, 5, 9788.

(40) Law, Y. T.; Zafeiratos, S.; Neophytides, S. G.; Orfanidi, A.; Costa, D.; Dintzer, T.; Arrigo, R.; Knop-Gericke, A.; Schlögl, R.; Savinova, E. R. *Chem. Sci.* **2015**, 6, 5635.

(41) Velasco-Velez, J.-J.; Pfeifer, V.; Hävecker, M.; Weatherup, R. S.; Arrigo, R.; Chuang, C.-H.; Stotz, E.; Weinberg, G.; Salmeron, M.; Schlögl, R.; Knop-Gericke, A. *Angew. Chem. Int. Ed.* **2015**, 54, 14554.

(42) Lichterman, M. F.; Hu, S.; Richter, M. H.; Crumlin, E. J.; Axnanda, S.; Favaro, M. et al. *Energy Environ. Sci.* **2015**, 8, 2409.

(43) Karslioglu, O.; Nemšák, S.; Zegkinoglou, I.; Shavorskiy, A.; Hartl, M.; Salmassi, F. et al. *Faraday Discuss.* **2015**, 180, 35.

(44) Favaro, M.; Jeong, B.; Yano, J.; Ross, P. N.; Hussain, Z.; Liu, Z.; Crumlin, E. J. *Nat. Commun.* **2016**, 7, 12695.

(45) Eilert, A.; Cavalca, F.; Robert, F. S.; Osterwalder, J.; Liu, C.; Favaro, M.; Crumlin, E. J.; Ogasawara, H.; Friebel, D.; Pettersson, L. G. M.; Nilsson, A. *J. Phys. Chem. Lett.* **2017**, 8, 285.

(46) Favaro, M.; Drisdell, W. S.; Marcus, M. A.; Gregoire, J. M.; Crumlin, E. J.; Haber, J. A.; Yano, J. *ACS Catalysis* **2017**, 7, 1248.

(47) Takagi, Y.; Wang, H.; Uemura, Y.; Nakamura, T.; Yu, L.; Sekizawa, O.; Uruga, T.; Tada, M.; Samjeské, G.; Iwasawa, Y.; Yokoyama, T. *Phys. Chem. Chem. Phys.* **2017**, 19, 6013.

(48) Favaro, M.; Valero-Vidal, C.; Eichhorn, J.; Toma, F. M.; Ross, P. N.; Yano, J.; Liu, Z.; Crumlin, E. J. *J. Mater. Chem. A* **2017**, DOI: 10.1039/c7ta00409e.

(49) Weiland, C.; Rumaiz, A. K.; Pianetta, P.; Woicik, J. C. *J. Vac. Sci. Tech. A* **2016**, 34, 030801.

(50) Starr, D. E.; Favaro, M.; Abdi, F. F.; Bluhm, H.; Crumlin, E. J.; van de Krol, R. *J. Electron Spectrosc. Relat. Phenom.* **2017**, DOI: 10.1016/j.elspec.2017.05.003.

(51) Nyholm, R.; Mårtensson, N.; Lebugle, A.; Axelsson, U. *J. Phys. F: Metal Phys.* **1981**,11, 1727.

(52) Becker, U.; Shirley, D. A. VUV and soft X-ray Photoionization. Plenum Press, New York (1996).

(53) Bocquet, A. E.; Mizokawa, T.; Saitoh, T.; Namatame, H.; Fujimori, A. *Phys. Rev. B* **1992**, 46, 3771.

(54) Biesinger, M. C.; Payne, B. P.; Grosvenor, A. P.; Lau, L. W. M.; Gerson, A. R.; Smart, R. St. C. *Appl. Surf. Sci.* **2011**, 257, 2717.

(55) Yang, J.; Liu, H.; Martens, W. N.; Frost, R. L. *J. Phys. Chem. C* **2010**, 114, 111.

(56) Weidler, N.; Paulus, S.; Schuch, J.; Klett, J.; Hoch, S.; Stenner, P. et al. *Phys. Chem. Chem. Phys.* **2016**, 18, 10708.

(57) Takata, Y.; Kayanuma, Y.; Yabashi, M.; Tamasaku, K.; Nishino, Y.; Miwa, D.; Harada, Y.; Horiba, K.; Shin, S.; Tanaka, S.; Ikenaga, E.; Kobayashi, K.; Senba, Y.; Ohashi, H.; Ishikawa, T. *Phys. Rev. B* **2007**, 75, 233404.

(58) Winter, B.; Weber, R.; Widdra, W.; Dittmar, M.; Faubel, M.; Hertel, I. V. *J. Phys. Chem. A* **2004**, 108, 2625.

(59) Nishizawa, K.; Kurahashi, N.; Sekiguchi, K.; Mizuno, T.; Ogi, Y.; Horio, T. et al. *Phys. Chem. Chem. Phys.* **2011**, 13, 413.

(60) Gaiduk, A.P.; Govoni, M.; Seidel, R.; Skone, J. H.; Winter, B.; Galli, G. *J. Am. Chem. Soc.* **2016**, 138, 6912.

(61) Langell, M. A.; Anderson, M. D.; Carson, G. A.; Peng, L.; Smith, S. *Phys. Rev. B* **1999**, 59, 4791.

(62) Smekal, W.; Werner, W. S. M.; Powell, C. J. *Surf. Interface Anal.* **2005**, 37, 1059.

(63) Werner, W. S. M.; Smekal, W.; Hisch, T.; Himmelsbach, J.; Powell, C. J. *J. Elect. Spectrosc. Relat. Phenom.* **2013**, 190, 137.

(64) Lin, F.; Klaus, S. W. *Nat. Chem.* **2014**, 13, 81.

(65) Zhang, M.; de Respinis, M.; Frei, H. *Nat. Chem.* **2014**, 6, 362.

(66) Pham, Hieu H.; Cheng, M.-J.; Frei, H.; Wang, L-W. *ACS Catal.* **2016**, 6, 5610.

(67) Pfeifer, V.; Jones, T. E.; Velasco Velez, J. J.; Arrigo, R.; Piccinin, S.; Hävecker, M.; Knop-Gericke, A.; Schlögl, R. *Chem. Sci.* **2017**, 8, 2143.

(68) McIntyre, N. S., Cook, M. G. *Anal. Chem.* **1975**, 47, 2208.

(69) Holm, R., Storp, S. *Appl. Phys.* **1976**, 9, 217.

(70) Dupin, J.-C.; Gonbeau, D.; Vinatier, P.; Levasseur, A. *Phys. Chem. Chem. Phys.* **2000**, 2, 1319.

(71) Koza, J. A.; Hull, C. M.; Liu, Y.-C.; Switzer, J. A. *Chem. Mater.* **2013**, 25, 1922.

(72) Tung, C.-W.; Hsu, Y.-Y.; Shen, Y.-P.; Zheng, Y.; Chan, T.-S.; Sheu, H.-S.; Cheng, Y.-C.; Chen, H. M. *Nat. Commun.* **2015**, 6:8106.

(73) Tougaard, S. *Surf. Sci.* **1989**, 216, 343.

(74) Evans, S. *Surf. Interface Anal.* **1991**, 17, 85.

(75) Muñoz-Flores, J.; Herrera-Gomez, A. *J. Electron Spectrosc. Relat. Phenom.* **2012**, 184, 533.

Table of Contents